

Oxophilicity and Structural Integrity in Maneuvering Surface Oxygenated Species on Nanoalloys for CO Oxidation

Shiyao Shan,[†] Valeri Petkov,[‡] Lefu Yang,^{†,§} Derrick Mott,^{||} Bridgid N. Wanjala,[†] Fan Cai,[§] Bing H. Chen,[§] Jin Luo,[†] and Chuan-Jian Zhong^{*,†}

[†]Department of Chemistry, State University of New York at Binghamton, Binghamton, New York 13902, United States

[‡]Department of Physics, Central Michigan University, Mt. Pleasant, Michigan 48859, United States

[§]College of Chemistry and Chemical Engineering, Xiamen University, Xiamen 361005, China

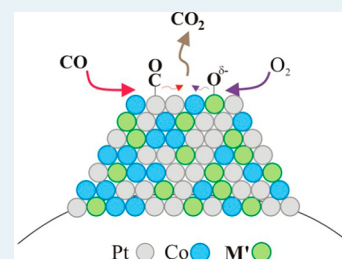
^{||}School of Materials Science, Japan Advanced Institute of Science and Technology, 1-1 Asahidai, Nomi, 923-1292 Ishikawa, Japan

Supporting Information

ABSTRACT: Platinum alloyed with transition metals at various compositions exhibits an enhanced catalytic activity for reactions involving oxygen activation, but little is known about the significance of oxophilicity that may play a role in maneuvering surface oxygenated species through the alloyed transition metal sites. Fundamental questions for sustainable high catalytic activity involve whether the oxygen activation or transfer occurring on the multicomponent particle surface induces any significant structural change of the nanoalloy in the catalytic process and how this is related to the oxophilicity. This paper addresses these questions by determining the catalytic activities of CO oxidation and the changes of the lattice parameters of nanoalloy particles in the catalytic processes as a function of the introduction of a third transition metal ($M' = V, Ni, Ir$, etc.) into PtCo nanoalloys. The results

reveal an activity enhancement of M' in the order of $V > Ni > Ir$, consistent with the order of oxophilicity of M' . In situ synchrotron high energy X-ray diffraction coupled to atomic pair distribution function analysis (HE-XRD/PDF) shows that the lattice parameter changes under CO oxidation conditions are very small for both PtVCo and PtNiCo nanoalloys. By comparing the changes in the lattice constant between PtVCo and PtNiCo in oxidation–reduction cycles under oxygen or hydrogen atmospheres, the former is also shown to exhibit a smaller change in lattice constant than those of the latter. The small change in the lattice parameter under CO reaction conditions is believed to reflect a surface self-regulation of the oxygenated species by the second and third transition metals in the nanoalloy (e.g., V and Co in PtVCo nanoalloy). Implications of the new insights into the unique integrity of the atomic-scale structure of platinum alloyed with transition metals are also discussed.

KEYWORDS: oxophilicity, oxygen activation, nanoalloys, CO oxidation, synchrotron high-energy X-ray diffraction, pair distribution function analysis



1. INTRODUCTION

Pt alloyed with transition metals at various compositions has been exploited extensively in heterogeneous catalysis. Little is known about the tunability of the metal's oxophilicity in the alloy that may play an important role in maneuvering surface oxygenated species in catalytic reactions involving oxygen reactants. For metals, oxophilicity is the tendency to form metal oxides by oxidation, hydrolysis, or abstraction of oxygen. In heterogeneous catalysis, oxophilicity of the catalyst is often determined by an oxide support. For example, for catalytic CO oxidation, one of the best documented catalysts is Au/TiO₂, which showed a 100% CO conversion at 0 °C.¹ In this example, CO activation occurs on Au sites, whereas oxygen activation happens along the peripheral (or premier) zone of Au/TiO₂. In numerous studies of AuM (e.g., AuAg)² alloys, oxygen activation is believed to occur on a Ag site, where the alloy is still supported on oxide-like support materials (even though the oxygen activation capability may be low). In contrast to most of the oxide supported nanoparticle catalysts,^{2,3} we report here a novel concept of self-tunable oxophilicity in Pt-transition metal

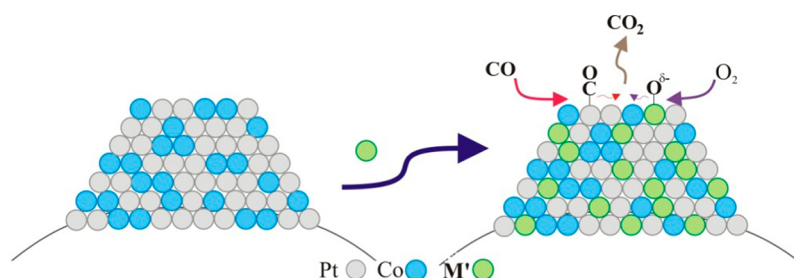
nanoalloys of binary (PtM) and ternary (PtMM') compositions supported on carbon. This concept is demonstrated by using CO oxidation as an example of catalytic reaction and introducing a third transition metal with different oxophilicity, forming PtMM' such as PtCoM' where $M' = V, Ni, Ir$, etc. PtNiCo/C and PtVCo/C catalysts treated under different thermochemical temperatures were recently shown to exhibit greatly enhanced electrocatalytic activity for oxygen reduction reaction in acidic electrolyte^{4–6} and for CO oxidation in the gas phase over PtNiCo supported on carbon, silica, and titania.⁷ In comparison with the other first-row transition metals, vanadium forms a variety of compounds in its many different oxidation states, and undergoes a wide variety of chemistry depending on the electronic and steric nature of the coordinating ligands. Importantly, vanadium in higher oxidation states is oxophilic but prefers donating ligands at low oxidation states.⁸ Co is also

Received: August 19, 2013

Revised: October 8, 2013

Published: November 22, 2013

Scheme 1. Schematic Illustration of the Introduction of a Third Transition Metal (M') into PtCo Nanoalloy, and the Surface Processes over PtCoM' Alloy Involving Formation/Removal of –O or –CO Species in CO Oxidation



oxophilic and its oxide form (either alone or as support) is also known to exhibit high activity to CO oxidation.^{3,9} V and Co would thus serve as ideal model M or M' to alloy with Pt in a study of the role of oxophilicity in the catalytic CO oxidation. One way to assess the oxophilicity is in terms of redox potential. For example, metals of Pt, Ni, Co, Ir, and V display the order of $V \gg Co \approx Ni > Pt$ and $Co \gg Ir$ in terms of oxophilicity. We demonstrate herein that the introduction of M' with oxophilicity larger (i.e., V) than Co results in a greater enhancement to the activity than introducing a metal (i.e., Ni) with oxophilicity close to Co. The understanding of this type of Pt-nanoalloy properties in terms of M or M' (Scheme 1) is useful for creating a bifunctional or multifunctional synergy for effective maneuvering of surface CO or oxygenated species over the M/M' sites through a structural or compositional effect.

Results from theoretical modeling have provided part of our rationale behind selecting the M/M' ratio in the nanoalloys. In addition to the theoretical insights in terms of the O₂ adsorption energy on different Pt alloys,^{10,11} one of our recent studies of ternary PtVFe nanoalloys¹² showed that, among three molecular chemisorption configurations known as Pauling, Griffith, and Yeager configurations, the O₂ bond is weakened the most with the Yeager configuration, followed by the Griffith and Pauling configurations. The charge transfer and the adsorption energy are dependent on the metal and adsorption site. In comparison with pure Pt clusters, PtVFe clusters were shown to be more effective in transferring electrons to O₂ species and thus weakening the O₂ bonds when the oxygen molecules bind to M and M' atoms. The electrocatalytic activity and stability are also related to the metal oxide formation for different transition metals.^{13,14} Indeed, for oxygen reduction reaction (ORR), the removal of O-containing intermediates (–O, –OH, –OOH) resulting from the O=O breaking on the Pt-bridge sites that recover the catalytically active sites has been shown to be more effective by alloying Pt with two different transition metal components (M and M') than with a single transition metal component. There are several recent studies supporting this hypothesis. In a study of Pt-trimetallic nanoalloy electrocatalysts for ORR prepared by electrodeposition,¹⁵ EXAFS and XPS characterization showed that the electronic states (e.g., d-band centers) and geometric factors (e.g., Pt–Pt distance) change with the composition. Also, recent DFT calculation of oxygen and hydroxyl adsorption energies showed that there is an approximate linear trend in oxygen reduction activity vs O or OH binding energy for a large number of different transition and noble metals.¹⁴ In a recent DFT study of the Pt₃Ni surface, negative Pt surface segregation energies were obtained when it is doped with a third transition metal (V, Fe, Co, Ir, etc.), whereas doping with Pd, Ag, and Au would completely suppress the Pt segregation.¹⁶

Despite these theoretical insights, a key question is how the oxygen species activation or transfer processes occurring on a multicomponent surface induce a change of the underlying lattice structure in the nanoparticles during the catalytic process. A change of the lattice structure in the nanoparticles could lead to a change in the surface catalytic activity and stability of the catalysts under catalytic reaction conditions. One approach to address this question is to determine changes in the lattice parameters of the nanoparticles during the catalytic processes. We have recently demonstrated the advantages of using high-energy X-ray diffraction coupled to atomic pair distribution function (HE-XRD/PDF) to probe the average atomic-scale structure, including changes in lattice parameters in binary/ternary nanoparticles^{7,17–21} and X-ray absorption fine structure spectroscopy (XAFS) to probe local atomic coordination structures in nanoparticles.^{6,7,18,21} In this report, we describe new findings from the use of HE-XRD/PDF for in situ probing of the lattice parameters and structural/chemical ordering of the nanoalloys in the catalytic CO oxidation reaction.

2. EXPERIMENTAL SECTION

Chemicals. Platinum(II) acetylacetonate (Pt(acac)₂, 97%) and nickel(II) acetylacetonate (Ni(acac)₂, anhydrous, >95%) were purchased from Alfa Aesar. Cobalt(III) acetylacetonate (Co(acac)₃, 99.95%) was purchased from Strem Chemicals. Iridium carbonyl (Ir₄(CO)₁₂, 98% pure), vanadyl acetylacetonate (VO(acac)₂, 98%), 1,2-hexadecanediol (90%), octyl ether ([CH₃(CH₂)₇]₂O, 99%), oleylamine (70%), and oleic acid (99+%) were purchased from Aldrich. Other solvents such as ethanol and hexane were purchased from Fisher Scientific. Gases of CO (1 vol % balanced by N₂) and O₂ (20 vol % balanced by N₂) were purchased from Airgas. All chemicals were used as received. Pt/C (particle size ~3 nm) was obtained from E-tek.

Nanoparticle Synthesis. The synthesis of PtCoM' nanoparticles where M' = V, Ni, Ir, etc., involved the reaction of three metal precursors in controlled molar ratios, the details of which were described in previous reports.^{6,7,18,21} PtCo and PtV nanoparticles were also synthesized similarly.²² For example, the synthesis of PtVCo nanoparticles involved the reaction of three metal precursors, Pt^{II}(acac)₂, V^{IV}O(acac)₂, and Co^{III}(acac)₃, in controlled molar ratios.²¹ These metal precursors were dissolved in an octyl ether solvent. A mixture of oleylamine and oleic acid was also dissolved in the solution and used as capping agents. 1,2-Hexadecanediol was used as a reducing agent for the reduction of the Pt-, V-, and Co-precursors. The formation of the oleylamine/oleic acid-capped PtVCo nanoparticles involves a combination of thermal decomposition and reduction reactions. In a typical procedure

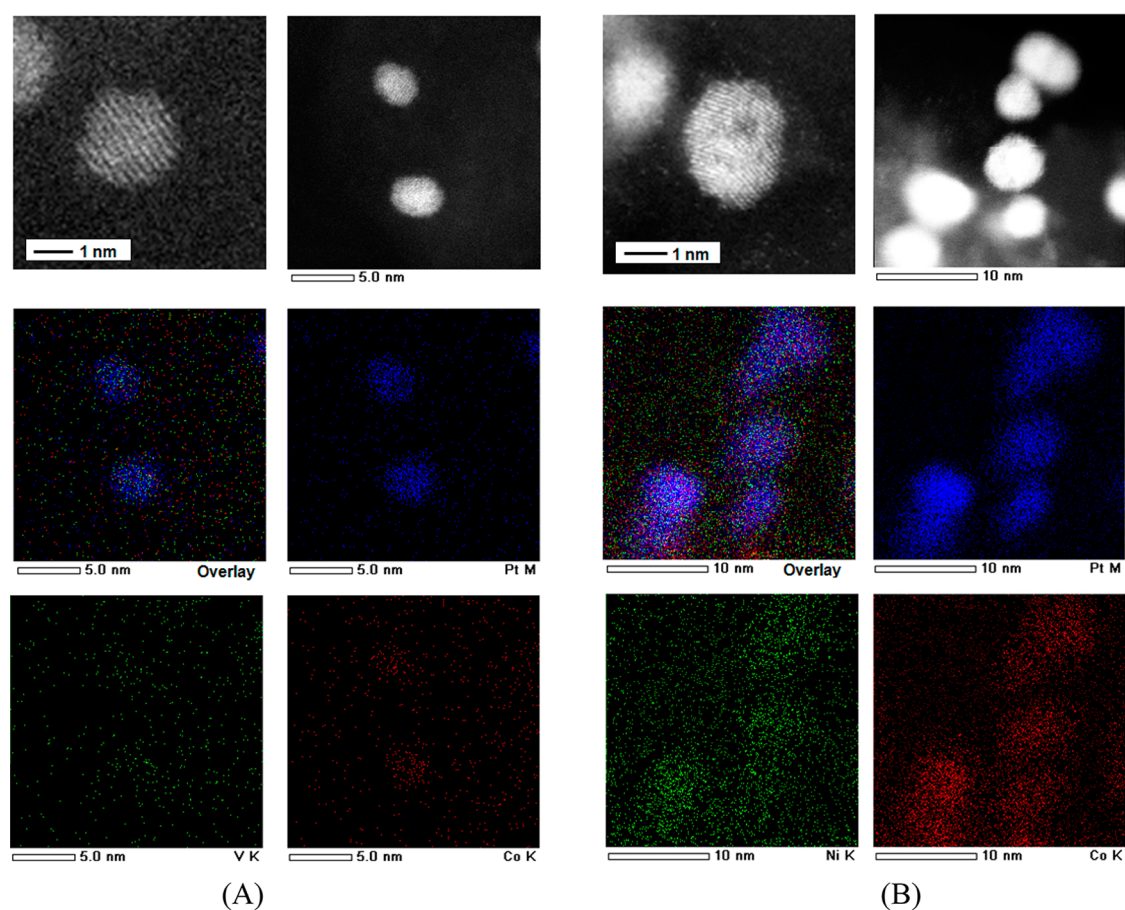


Figure 1. High-angle annular dark field scanning TEM (HAADF-STEM) images: morphological imaging and elemental mapping for Pt₄₅V₁₈Co₃₇/C (A) and Pt₂₅Ni₁₆Co₅₉/C (B).

for the synthesis of Pt₄₅V₁₈Co₃₇, for example, 1,2-hexadecanediol (2.5 mmol), Pt(acac)₂ (1.97 mmol), VO(acac)₂ (0.935 mmol), Co(acac)₃ (1.934 mmol), oleylamine (2.13 mmol), and oleic acid (3.13 mmol) were mixed in 120 mL of octyl ether in a three-neck 1 L flask under stirring. The solution was first purged with N₂ and heated to 105 °C, and then heated to 270 °C and refluxed for 40 min. After the reaction mixture was allowed to cool down to room temperature, the product was precipitated by adding ethanol. The black precipitate was completely dried under nitrogen and dispersed in a known amount of hexane.

Catalyst Preparation. For the preparation of carbon supported nanoparticles, a typical procedure involved suspending ~800 mg of carbon black (Ketjen Black) in 500 mL of hexane containing ~200 mg of nanoparticles followed by stirring for ~15 h. The resulted powder was collected and dried under N₂.

The supported catalysts were further treated in a quartz tube furnace. The nanoparticles supported on carbon were first heated at 260 °C in 15 vol % O₂ (oxidative atmosphere) for 30 min for removing the organic capping molecules and then treated at 400 °C in 15 vol % H₂ for 120 min. The capping molecules were removed effectively by the thermal treatment.^{21,23} The weight loadings of the carbon supported catalysts were 20% for most of the catalysts studied in this work, including Pt₄₅V₁₈Co₃₇/C, Pt₂₅Ni₁₆Co₅₉/C, Pt₃₉Ni₂₂Co₃₉/C, Pt₂₃Ir₂₉Co₄₈/C, Pt₅₅Co₄₅/C, and commercial Pt/C, unless otherwise noted (35% for Pt₆₁V₃₉/C). Thermogravimetric

analysis (TGA) was performed on a Perkin-Elmer Pyris 1-TGA for determining the actual loading of metals on the carbon support. The particle sizes of the carbon-supported catalysts were 3.3 ± 0.7 nm for Pt₄₅V₁₈Co₃₇/C, 4.4 ± 0.5 nm for Pt₃₉Ni₂₂Co₃₉/C, 3.5 ± 0.4 nm for Pt₂₅Ni₁₆Co₅₉/C, 3.3 ± 0.6 nm for Pt₂₃Ir₂₉Co₄₈/C, 3.9 ± 0.7 nm for Pt₅₅Co₄₅/C, and 5.7 ± 1.0 nm for Pt₆₁V₃₉/C.

Catalytic Activity Measurement. The catalytic activity of the catalysts for CO (0.5 vol %) + O₂ (10 vol %) reaction (balanced by N₂) was measured using a custom-built system including a temperature-controlled reactor, gas flow/mixing/injection controllers, and an online gas chromatograph (Shimadzu GC 8A) equipped with 5A molecular sieve and Porapak Q packed columns and a thermal conductivity detector. The catalysts were loaded in a quartz microreactor tube (inner diameter: 4 mm) and wrapped by quartz wool in the middle of the tube (length of the catalyst bed: 6 mm). The feeding gas (0.5 vol % CO + 10 vol % O₂ balanced by N₂) was injected continuously through the fixed catalyst bed in the quartz microreactor at a flow rate of 20 mL/min. The residence time was about 0.2 s. The gas hourly space velocity (GHSV) in our system is around 16 000 h⁻¹. Temperature control was achieved by a furnace and a dry ice sheath coupled with a temperature controller. The catalytic activity for CO oxidation was determined by analyzing the composition of the tail gas effusing from the quartz microreactor packed with the catalyst fixed bed by the online gas chromatograph.

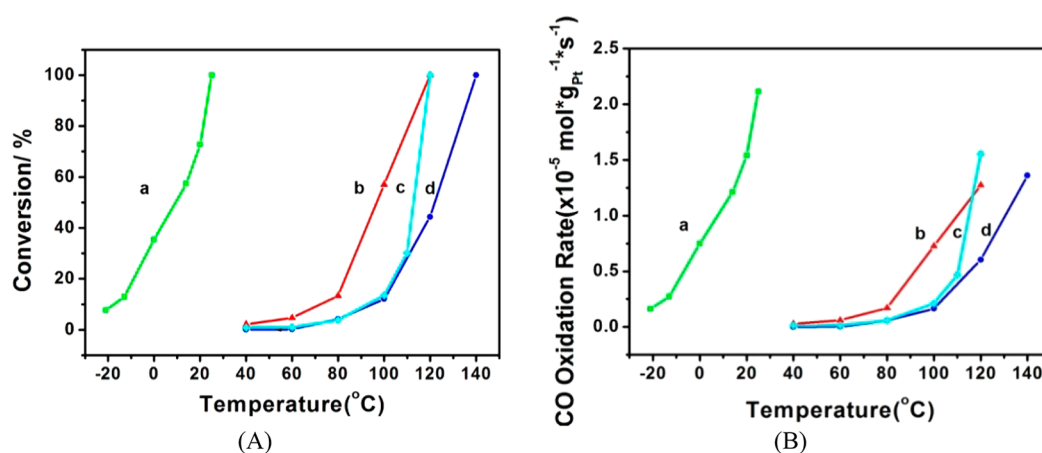


Figure 2. CO conversion % (A) and rate (B) as a function of the reaction temperature for $\text{Pt}_{45}\text{V}_{18}\text{Co}_{37}/\text{C}$ (green, a), $\text{Pt}_{55}\text{Co}_{45}/\text{C}$ (red, b), $\text{Pt}_{61}\text{V}_{39}/\text{C}$ (light blue, c), and Pt/C (blue, d) catalyst prepared by treatment at 260 °C under 20 vol % O_2 (oxidative) followed by treatment at 400 °C in 15 vol % H_2 (reductive) in a programmatic furnace. (The standard deviation of the data is $\pm 0.3\%$, with an RSD of 0.4%.)

Morphology and Composition Characterization. High-angle annular dark-field scanning TEM (HAADF-STEM) imaging for morphology characterization and energy dispersive X-ray spectroscopy (EDS) for elemental mapping were carried out on a JEOL JEM-ARM200F instrument operated at 200 kV with a spherical aberration corrector. The nanoparticle samples were suspended in hexane solution and were drop cast onto a carbon-coated copper grid followed by solvent evaporation in ambient atmosphere at room temperature.

Inductively Coupled Plasma-Optical Emission Spectroscopy (ICP-OES). ICP-OES was used to analyze the composition. It was performed on a Perkin-Elmer 2000 DV ICP-OES instrument utilizing a cross-flow nebulizer with the following parameters: plasma 18.0 L of $\text{Ar}_{(\text{g})}/\text{min}$; auxiliary 0.3 L of $\text{Ar}_{(\text{g})}/\text{min}$; nebulizer 0.73 L of $\text{Ar}_{(\text{g})}/\text{min}$; power 1500 W; peristaltic pump rate 1.40 mL/min. Elements $<1.0 \text{ mg/L}$ were analyzed using a Meinhardt nebulizer coupled to a cyclonic spray chamber to increase analyte sensitivity with the following parameters: 18.0 L of $\text{Ar}_{(\text{g})}/\text{min}$; auxiliary 0.3 L of $\text{Ar}_{(\text{g})}/\text{min}$; nebulizer 0.63 L of $\text{Ar}_{(\text{g})}/\text{min}$; power 1500 W; peristaltic pump rate 1.00 mL/min. Laboratory check standards were analyzed for every 6 or 12 samples, with instrument recalibration if check standards were not within $\pm 5\%$ of the initial concentration. Note that the composition of the supported nanoparticles after thermal treatment was sometimes slightly different ($<10\%$) from that of the as-synthesized nanoparticles, which were largely due to different degrees of losses of metals into the supporting materials during ICP sample preparation.

In Situ and Ex Situ Characterization Using Synchrotron High-Energy XRD (HE-XRD). HE-XRD measurements were carried out in both ex situ ($\lambda = 0.1080 \text{ \AA}$) and in situ ($\lambda = 0.1378 \text{ \AA}$) modes on beamlines 11-ID-C and 11-ID-B, respectively, at the Advanced Photon Source, Argonne National Laboratory. In situ experiments were performed with a reactor type cell described by Oxford et al.²⁴ The catalyst sample was loaded into a glass capillary with a length of 10 cm and a diameter of 1 mm wrapping by quartz wool on each end. The capillary was then loaded into the in situ flow cell on beamline 11-ID-B at the Argonne National Lab which allows for controlling the gas environment and the sample temperature by flow and temperature controller (see Scheme S1, Supporting Information).

The XRD diffraction data were reduced to the so-called structure factors, $S(q)$, and then Fourier transformed to atomic PDFs, $G(r)$, using the relationship

$$G(r) = \frac{2}{\pi} \int_{q=0}^{q_{\text{max}}} q[S(q) - 1] \sin(qr) dq \quad (1)$$

where $q_{\text{max}} = 25 \text{ \AA}^{-1}$ in the present experiments. The wave vector q is defined as $q = 4\pi \sin(\theta)/\lambda$, where θ is half of the scattering angle and λ is the wavelength of the X-rays used. Note, as derived, atomic PDFs $G(r)$ are experimental quantities that oscillate around zero and show positive peaks at real space distances, r , where the local atomic density $\rho(r)$ exceeds the average one ρ_0 . This behavior can be expressed by the equation $G(r) = 4\pi r \rho_0 [\rho(r)/\rho_0 - 1]$, which is the formal definition of the PDF $G(r)$. High-energy XRD and atomic PDFs have already proven to be very efficient in studying the atomic-scale structure of nanosized materials.^{25,26}

3. RESULTS AND DISCUSSION

Figure 1A shows a representative set of high-angle annular dark-field scanning TEM (HAADF-STEM) and energy dispersive X-ray spectroscopy (EDS) images for a sample of $\text{Pt}_{45}\text{V}_{18}\text{Co}_{37}$ supported on carbon after thermochemical processing. While the resolution is still limited in the HAADF images, the crystalline features can be clearly seen, showing no apparent indication of phase segregation. In the EDS mapping images, the overlap of the Pt, V, and Co metal distribution shows a good degree of alloying across the entire nanoparticle. Similar results were obtained with $\text{Pt}_{25}\text{Ni}_{16}\text{Co}_{59}/\text{C}$ (Figure 1B). Note that the scattering of the data points in the EDS images was likely due to thermal diffuse scattering under the imaging condition.

More details from the characterizations of the nanoalloy catalysts with XRD, XPS, and other techniques have been reported in our recent studies in relation to the electrocatalytic properties of the catalysts.^{6,7,18,21} This paper focuses on a comparison of the catalytic properties in correlation with the lattice parameters of the nanoalloys under reaction conditions.

Catalytic Activity for CO Oxidation Reaction. The exemplary data for the catalytic properties shown here concentrate on the comparison between the CO conversion rates of PtCo and those for PtCoM'. The first example of M' is V (Figure 2). In Figure 2B, the CO oxidation rates of PtVCo/C

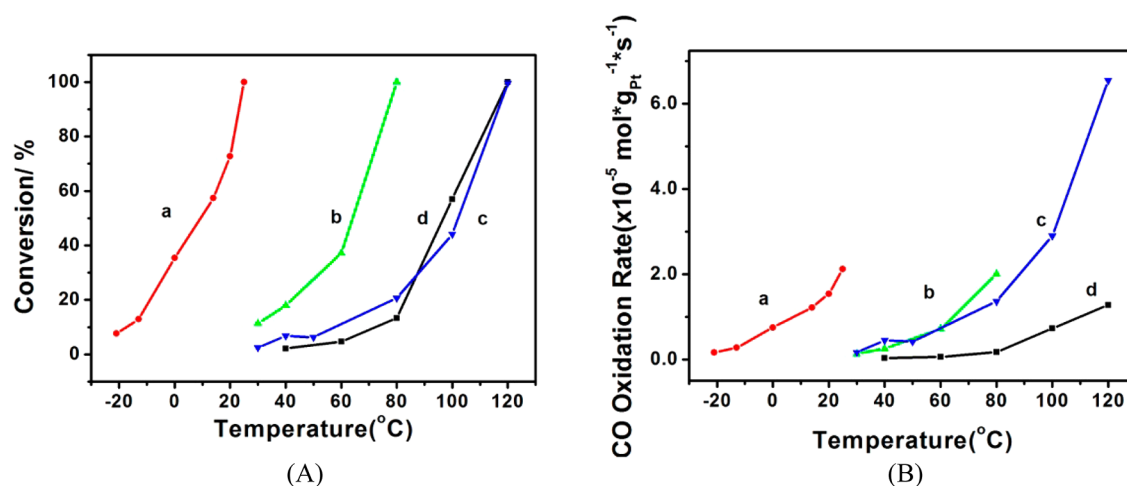


Figure 3. Comparisons of CO conversion % (A) and oxidation rate (B) over Pt₄₅V₁₈Co₃₇/C (red, a), Pt₃₉Ni₂₂Co₃₉/C (green, b), and Pt₂₃Ir₂₉Co₄₈/C (blue, c) with Pt₅₅Co₄₅/C (black, d) catalysts. The Pt mass specific CO oxidation rate is normalized against the metal loading on carbon and the Pt composition in the nanoparticles.

Table 1. Comparison of Kinetic Data of the Different Nanoalloy Catalysts

catalysts	d_{NPs}^c (nm)	thermal treatment ^c	reaction rate ^a [$\times 10^{-6}$ mol/(g _{pt} ·s)] (80 °C)	ave. D^b (dispersion, %)	TOF ^d ($\times 10^{-2}$ s ⁻¹)	E_a (kJ mol ⁻¹)
Pt/C	2.5–3.0	O ₂ –H ₂	0.57	42	0.027	80.9
Pt ₅₅ Co ₄₅ /C	3.9 ± 0.7	O ₂ –H ₂	1.70	29	0.11	51.8
Pt ₆₁ V ₃₉ /C	5.7 ± 1.0	O ₂ –H ₂	0.59	20	0.058	80.3
Pt ₄₅ V ₁₈ Co ₃₇ /C	3.3 ± 0.7	O ₂ –H ₂	21.2 ^f	35	1.17	34.0
Pt ₃₉ Ni ₂₂ Co ₃₉ /C	4.4 ± 0.5	O ₂ –H ₂	>20.1	26	1.53	48.2
Pt ₂₃ Ir ₂₉ Co ₄₈ /C	3.3 ± 0.6	O ₂ –H ₂	13.6	34	0.77	40.0

^aThe calculation of the reaction rate was based upon the moles of CO reacted at the flow rate and was normalized against the total mass of Pt in the catalyst. All nanoparticles are random alloys. ^bThe dispersion of Pt on the surface of one nanoparticle was calculated by using $D = (6V_m)/(a_m d) \times 100\%$. V_m is the volume of atom Pt, and a_m is the Pt surface area. ^c d_{NPs} or d is the particle size. ^dThe calculation of TOF was based on the surface Pt. TOF = reaction rate/(MW(Pt) × D). Note that the metal loading was mostly 20%, which is significantly higher than usual (0.1–8%), leading to a higher percentage of buried nanoparticle surface. ^eThe catalyst was treated at 260 °C under 20 vol % O₂ followed by treatment at 400 °C in 15 vol % H₂. ^fThe result was obtained at 23 °C.

catalyst are compared with those for PtCo/C and PtV/C catalysts at different reaction temperatures in terms of Pt-specific mass activity. Data for a sample of commercial Pt/C catalyst is also included for comparison. The comparison illustrates the relative enhancement of the catalytic activity of ternary nanoparticles compared to the binary ones and Pt. In this example, the catalysts were subjected to the same thermochemical treatments involving heating at 260 °C under O₂ atmosphere and then at 400 °C under H₂ atmosphere followed by exposure to ambient atmosphere before use. In comparison with Pt/C and the binary counterparts, the ternary PtVCo/C catalyst shows a significantly enhanced catalytic rate for CO oxidation. In Figure 2A, it exhibits ~40% CO conversion at 0 °C, which is somewhat lower than that of the best Au/TiO₂ catalyst for CO oxidation which could show 100% conversion at 0 °C.¹ At this temperature, Pt/C, PtCo/C, and PtV/C showed basically no catalytic activity. At relatively low temperatures (e.g., 40 °C), the activity of PtVCo/C is greater than that of PtCo/C by a factor of 10²–10³. This is a remarkable enhancement of CO oxidation activity. On the other hand, the activity of PtCo/C is greater than that of PtV/C or Pt/C by a factor of ~10. It should also be noted that the ternary catalyst is remarkably stable because there is only a slight decrease (about 15%) in activity for over 2 days when the catalyst is exposed to the gas reactants (0.5 vol % CO and 10 vol % O₂).

The catalytic activity of PtVCo/C catalyst is further compared with those for PtNiCo/C⁷ and PtIrCo/C catalysts (Figure 3). It is evident that the PtVCo/C exhibits the highest activity, in the order PtVCo ≫ PtNiCo > PtIrCo ≥ PtCo. At room temperature, the activity of PtVCo/C is greater than that of PtNiCo/C by a factor of 10–20. In comparison with PtCo/C, the addition of V into the binary system leads to an increase in the activity by a factor of 10²–10³, whereas the addition of Ni into the binary system leads to an increase in the activity by a factor of 10–20. The addition of Ir into the binary system showed the smallest increase in the catalytic activity. The catalytic activity order PtVCo ≫ PtNiCo > PtIrCo ≥ PtCo appears to be consistent with the order of oxophilicity of the third transition metal (M') in PtCoM' (M' = Ni, V, and Ir), which is in the order of V > Ni > Ir.

Table 1 summarizes kinetic data such as the turnover frequency (TOF) and the activation energy (E_a) derived from the CO conversion data for the catalysts tested under our experimental conditions. Since the catalytic reaction was measured at a “steady state” at a selected temperature, not in a way where the temperature was continuously changed, the data at T_{10} , i.e., the temperature corresponding to 10% CO conversion, was used as a measure of the light off temperature. The values of T_{10} (see Table S1, Supporting Information) showed significant differences among the nanoalloys studied in this work. Note that the metal loading for the catalysts studied in this work was mostly 20% (wt), which is much larger than

the usual (0.1–8%), leading to a higher percentage of buried nanoparticle surfaces, which is mainly responsible for the relatively low TOF and high E_a . This was in fact confirmed by a comparison of the CO conversion data of carbon-supported Pt₅₅Co₄₅ catalysts with two different loadings: 1% (wt) and 20% (wt) (see Tables S1–2, Supporting Information). The data showed that the TOF for the catalyst with 1% loading ($2.1 \times 10^{-1} \text{ s}^{-1}$) is about 1 order of magnitude higher than that for the catalyst with 20% loading ($1.2 \times 10^{-2} \text{ s}^{-1}$), which is consistent with a better and higher utilization of the surface sites of the nanoparticles for the former.

Since this report focuses on a comparison of the catalytic activities among the different catalysts under the same experimental conditions with the synchrotron HE-XRD measurement which requires a higher loading in order to produce good signal-to-noise ratio data, we focused on the study of the catalysts with 20% loading for an effective assessment of the structure–activity correlation. In general, while PtCo shows a higher catalytic activity than pure Pt catalyst in terms of an increased TOF and lowered E_a , the introduction of a third transition metal M' (V, Ni, Ir) into the PtCo alloy leads to a further significant increase in TOF and lowering of E_a , as demonstrated by the activity order of Pt₄₅V₁₈Co₃₇/C > Pt₃₉Ni₂₂Co₃₉/C > Pt₂₃Ir₂₉Co₄₈/C > Pt₅₅Co₄₅/C. Note that the high TOF and low E_a reported for Pt₄₅V₁₈Co₃₇ are based on the catalytic data taken at room temperature. Binary PtV/C showed only a slight or insignificant increase of TOF and lowering of E_a when compared to Pt/C.

The possibility of deactivation of the ternary catalysts is also found to depend on the nature of the third metal, as evidenced by a comparison of the deactivation behavior of PtVCo/C and PtNiCo/C catalysts in CO oxidation (Figure 4). The PtVCo

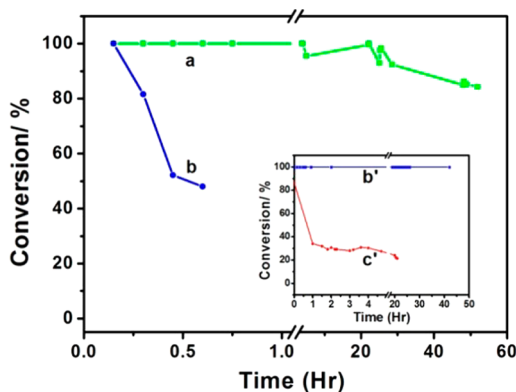


Figure 4. Comparison of CO conversion % data as a function of reaction time: Pt₄₅V₁₈Co₃₇/C (green, a) and Pt₂₅Ni₁₆Co₅₇/C (blue, b) catalysts at 23 °C. Inset: a comparison of the activity of Pt₂₅Ni₁₆Co₅₇/C (blue, b') with Pt₂₃Ir₂₉Co₄₈/C (red, c') catalyst at 100 °C.

nanoalloy's activity was found to sustain for a longer period of time than those for the PtNiCo/C and PtCo/C nanoalloys. At room temperature (23 °C), the catalytic activity drop is only about 4% for PtVCo/C after 28 h of reaction under 0.5 vol % CO and 10 vol % O₂. After 52 h, the CO conversion showed still very good activity and 85% CO conversion. For PtNiCo, initially a 100% CO conversion is reached after a thermal treatment under 15% H₂ at 400 °C for 2 h, but it drops down to 40% within 30 min at room temperature. A similar initial high activity is also shown when the support is TiO₂, but it drops to around 15% conversion after 48 h.⁷ There is a clear

reduction of the deactivation for the PtVCo/C catalyst in comparison with that for PtNiCo/C. To further compare the activity with other nanoalloys, data taken at higher reaction temperatures must be used, at which PtNiCo shows 100% CO conversion. As shown by the inset in Figure 4, comparing the activities of PtIrCo/C and PtNiCo/C over time at a relatively high temperature (100 °C), the PtNiCo/C shows a lesser propensity of deactivation than PtIrCo/C.

The data demonstrate that the addition of a third metal such as Ni, V, or Ir into PtCo leads to significant differences in both catalytic activity and propensity of deactivation. One way to assess these differences is to consider the transition metal oxophilicities in terms of the redox potential (E^0). For example, under basic conditions, Co is more oxophilic than Pt in terms of E^0 's ($E^0(\text{Co(II)-OH}/\text{Co(0)}) = -0.73 \text{ V} < E^0(E^0(\text{Pt(II)-OH}/\text{Pt(0)}) = 0.14 \text{ V}$). In comparison with Co, the oxophilicity of Ni ($E^0(\text{Ni(II)-OH}/\text{Ni(0)}) = -0.72 \text{ V}$) is very close to that for Co species, whereas $E^0(\text{V(V)-O}/\text{V(0)}) = -2.19 \text{ V}$ is much more negative than those for Co and Ir species ($E^0(\text{Ir(III)-O}/\text{Ir(0)}) = 0.098 \text{ V}$). Our results clearly demonstrate that the introduction of a third metal with oxophilicity larger (e.g., V) than Co results in a great enhancement in the catalytic activity in the resulted PtVCo nanoalloy, which is consistent with the oxophilicity difference between V and Co ($E^0(\text{V}) \ll E^0(\text{Co})$). The oxophilicity of Ni is close to Co, endowing PtNiCo with a higher activity than PtCo. The oxophilicity of Ir is smaller than that of both Ni and V, enabling PtIrCo with a smaller increase in activity than PtCo.

HE-XRD and Atomic PDF Characterization. The nanoalloy catalysts were characterized by in situ HE-XRD measurements in several reactive atmospheres, including a gas mixture of CO and O₂, and oxidative (O₂) or reductive (H₂) gas, at different temperatures. The in situ study focused on the PtVCo catalyst system. Some comparisons (in situ or ex situ) were also made with data for PtNiCo and PtIrCo catalysts.

Structural Characteristics of Nanoalloys under Catalytic Reaction Conditions (in a Gas Mixture of CO and O₂). Figure 5 shows a representative set of HE-XRD patterns (A) and the respective atomic PDFs (B) for Pt₄₅V₁₈Co₃₇/C under a gas mixture of CO and O₂. Two samples were examined. The first was a fresh catalyst prepared by thermal treatment at 260 °C under 20 vol % O₂ (oxidative) followed by treatment at 400 °C in 15 vol % H₂ (reductive), which was then tested in a gas mixture of 2.5 vol % CO and 10 vol % O₂ (top panel). The second was an aged catalyst, which was first exposed to CO + O₂ atmosphere at 80 °C for 1 h. The catalyst was then subjected to HE-XRD experiments in a reductive gas (5 vol % H₂) atmosphere at different temperatures (bottom panel). Measurement sequences involved starting from room temperature (RT, 25 °C), heating at a certain temperature, and then cooling back to RT. The XRD patterns (A) show broad diffraction features that are typical for nanosized particles. As can be seen in Figure 5B, the respective PDFs show a sequence of sharp peaks, reflecting the presence of well-defined atomic coordination spheres in the samples studied, allowing convenient testing and refinement of structure models. The radii of the coordination spheres can be estimated from the positions of the respective PDF peaks, and the respective coordination numbers from the areas of those peaks. The real space distance at which the atomic PDF decays to zero is a measure of the so-called length of structural coherence, also known as coherently scattering domain size. In particular, the peaks in the experimental PDFs in Figure 5B show up to a real

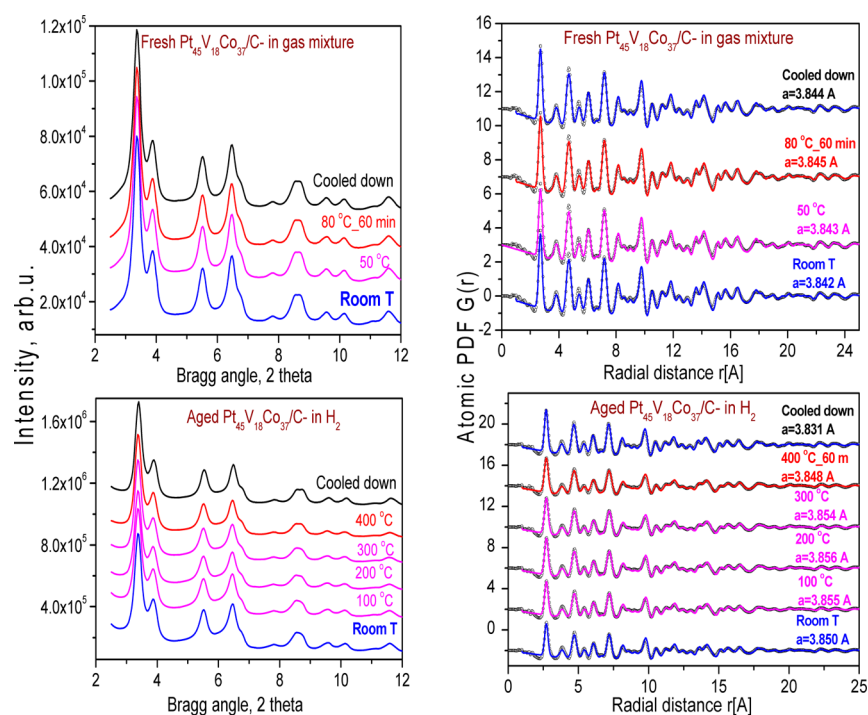


Figure 5. In situ HE-XRD data. XRD patterns taken with X-rays of wavelength 0.13072 Å (A) and atomic PDFs (B) for two samples of $\text{Pt}_{45}\text{V}_{18}\text{Co}_{37}/\text{C}$ (experimental PDFs, symbols; model PDFs, solid lines). Top panel: a fresh sample (prepared by treatment at 260 °C under 20 vol % O_2 (oxidative) followed by treatment at 400 °C in 15 vol % H_2 (reductive)) in a gas mixture (2.5 vol % CO + 10 vol % O_2 balanced by N_2). Bottom panel: an aged catalyst, which was first exposed to CO + O_2 mixed gas at 80 °C for 1 h and then subjected to HE-XRD experiments in a reductive gas (5 vol % H_2) at different temperatures. Measurement sequences involved starting from room temperature (25 °C), heating at a certain temperature, and then cooling back to room temperature. (The standard deviation of lattice constant a : ± 0.004 (RSD: 0.1%).)

space distance of about 25–35 Å, which may be considered as a length of structural coherence in the nanoalloy particles studied here. That length is comparable to but less than the particles' size (~ 4 nm) determined by TEM, indicating the presence of non-negligible local atomic disorder in the nanoalloys. The presence of such disorder is typical for metallic particles a few nanometers in size and usually is due to surface relaxation effects.^{27,28}

The atomic PDFs for the two (fresh and aged) samples of $\text{Pt}_{45}\text{V}_{18}\text{Co}_{37}/\text{C}$ nanoalloys are compared to assess the effect of the thermochemical treatment condition and reactive atmosphere on the atomic-scale structure. The atomic PDFs were approached with structure models to reveal finer details of the atomic arrangement in the respective nanoalloys. The fits were done with the help of the program PDFGui.²⁹ There are two major findings. First, in mixed gases (2.5 vol % CO and 10 vol % O_2), the lattice constant shows little change. It is 3.842 Å at RT, 3.845 Å at 80 °C, and 3.844 Å when the sample is cooled back down to RT. Second, under the reducing gas (5 vol % H_2), there is a considerable shrinking of the lattice constant from 3.850 Å at RT to 3.848 Å at 80 °C, and to 3.831 Å when the sample is cooled back to RT.

A similar in situ experiment was performed for $\text{Pt}_{25}\text{Ni}_{16}\text{Co}_{59}/\text{C}$ catalysts. The HE-XRD patterns (A) and the respective atomic PDFs (B) under a gas mixture of CO and O_2 and in reducing gas (H_2) atmosphere are shown in Figure 6. As can be seen in the figure (top panel), little structural change is seen when the catalyst is subjected to a gas mixture of CO and O_2 at 80 °C. In particular, the change in the lattice constant is relatively small when the temperature is changed from RT (3.885 Å) to 80 °C (3.887 Å), and then back to RT (3.886 Å). However, upon exposing to H_2 gas atmosphere at 400 °C, the

change is noticeable, as evidenced by the difference of the respective lattice constants: from 3.861 Å at RT to 3.856 Å at 100 °C, then to 3.851 Å at 200 °C, 3.846 Å at 300 °C, 3.828 Å at 400 °C, and to 3.851 Å when the sample is cooled to RT.

Structural Characteristics of Nanoalloys in Oxidative (O_2) or Reductive (H_2) Gas. To understand the effects of the oxidative or reductive atmosphere on the catalyst structure, we further examined the $\text{Pt}_{45}\text{V}_{18}\text{Co}_{37}/\text{C}$ nanoalloys in oxidative (10 vol % O_2) or reductive (3.5 vol % H_2) gas at different temperatures. Figure 7 shows a representative set of in situ HE-XRD data for $\text{Pt}_{45}\text{V}_{18}\text{Co}_{37}/\text{C}$ (A) and the respective atomic PDFs (B).

As reported in our recent study,²¹ the PDF for the sample treated at relatively low temperature (e.g., 400 °C) can be equally well described with structure models featuring a random $\text{Pt}_{45}\text{V}_{18}\text{Co}_{37}/\text{C}$ alloy fcc type or chemically ordered alloy fct type structure, in comparison with PDF for pure Pt which can be very well fit with a structure model featuring an fcc type structure with a parameter of 3.92 Å. The PDF refined fct lattice parameters for the sample treated at 400 °C are $a = 2.710$ Å and $c = 3.776$ Å. Note that the chemically ordered fct lattice model becomes increasingly a better match to the experimental PDFs for the particles annealed at >400 °C. If Pt/C and $\text{Pt}_{45}\text{V}_{18}\text{Co}_{37}/\text{C}$ samples are compared on the basis of a hypothetical fcc model, the respective lattice parameters change from $a = 3.820$ Å (400 °C) to $a = 3.809$ Å (600 °C), revealing that the $\text{Pt}_{45}\text{V}_{18}\text{Co}_{37}/\text{C}$ catalysts undergo a phase transition from a random alloy to a chemically ordered alloy type structure and an associated shrinking of the distances between the metal atoms.

On the basis of the final room temperature data after the O_2 or H_2 treatments, the changes in lattice parameter are

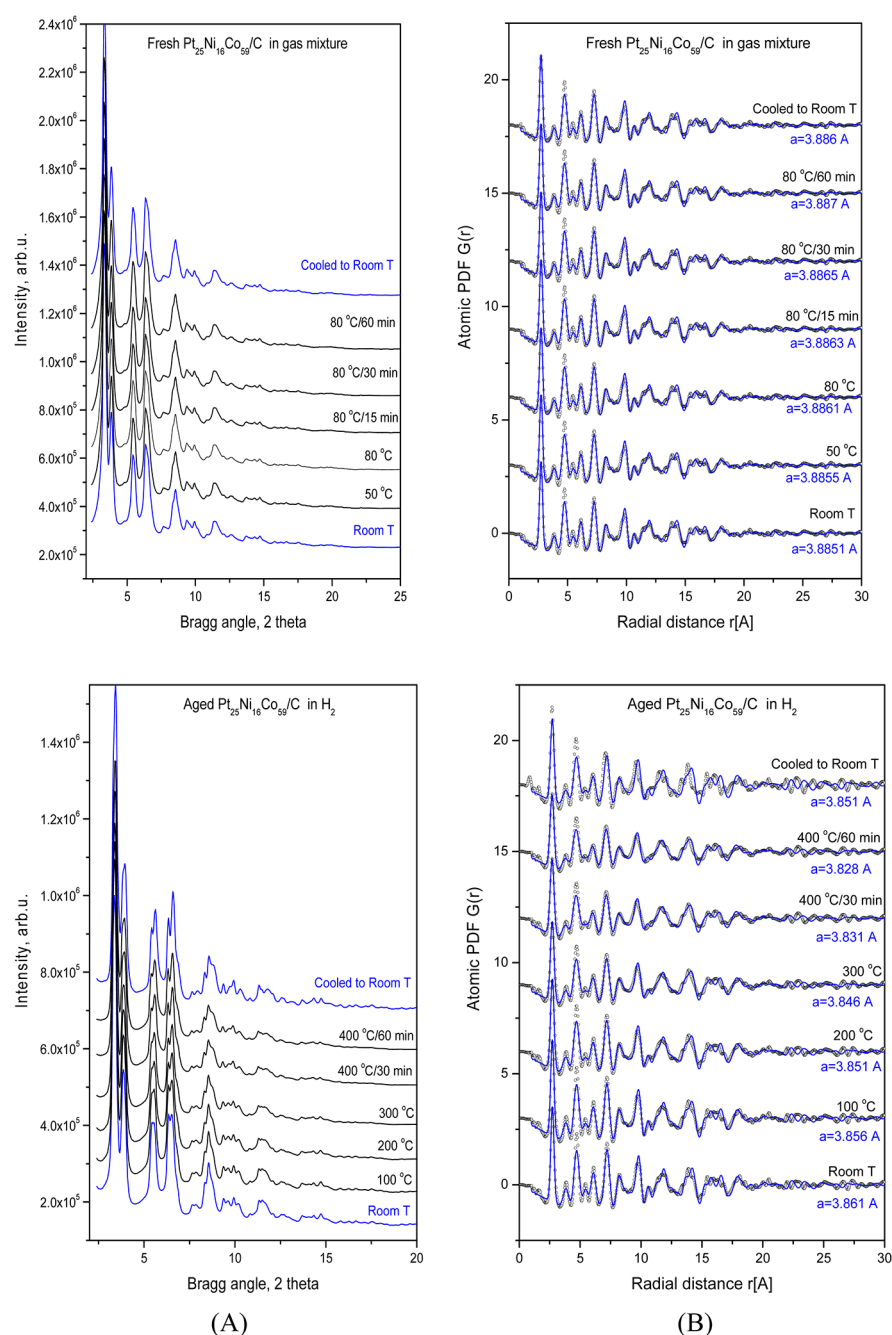


Figure 6. In situ HE-XRD data. XRD patterns taken with X-rays of wavelength 0.13072 Å (A) and atomic PDF data (B) for two samples of $\text{Pt}_{25}\text{Ni}_{16}\text{Co}_{59}/\text{C}$ (experimental PDF data, symbols; model PDF data, solid lines). Top panel: a fresh sample (prepared by treatment at 260 °C under 20 vol % O_2 (oxidative) followed by treatment at 400 °C in 15 vol % H_2 (reductive)). Bottom panel: an aged catalyst, which was tested first in CO + O_2 mixed gas (80 °C) for 1 h and then was subjected to HE-XRD experiments in a reductive gas (5 vol % H_2) atmosphere at different temperatures. In part B, symbols are for the experimental data and solid lines for the fitted models.

compared between O_2 and H_2 treated PtVCo catalyst and its binary counterparts (PtV and PtCo) (Table S3, Supporting Information); the change in lattice for PtCo is slightly smaller than that for the PtVCo. Interestingly, a much smaller change in lattice parameter is observed for the PtV catalyst. In terms of TOFs, the data displays the order of $\text{Pt}_{45}\text{V}_{18}\text{Co}_{37} > \text{Pt}_{55}\text{Co}_{45} > \text{Pt}_{61}\text{V}_{39}$ (Table S3, Supporting Information). Clearly, the addition of V into PtCo may have played a role in limiting the expansion/shrinking under oxidative/reductive treatment conditions. As will be discussed next, this finding is in contrast

to the addition of Ni to PtCo, which does not show this capability.

For a comparison with the above data, we also examined PtNiCo/C catalysts in oxidative (O_2) or reductive (H_2) gas at different temperatures. Figure 8 shows a representative set of experimental in situ HE-XRD data for $\text{Pt}_{25}\text{Ni}_{16}\text{Co}_{59}/\text{C}$ (A) and the respective atomic PDFs (B).

On the basis of the data shown in Figures 7 and 8, the changes of the lattice parameters in the oxidation–reduction cycles are compared between the PtVCo and PtNiCo systems (Figure 9). One intriguing finding is that the changes in the

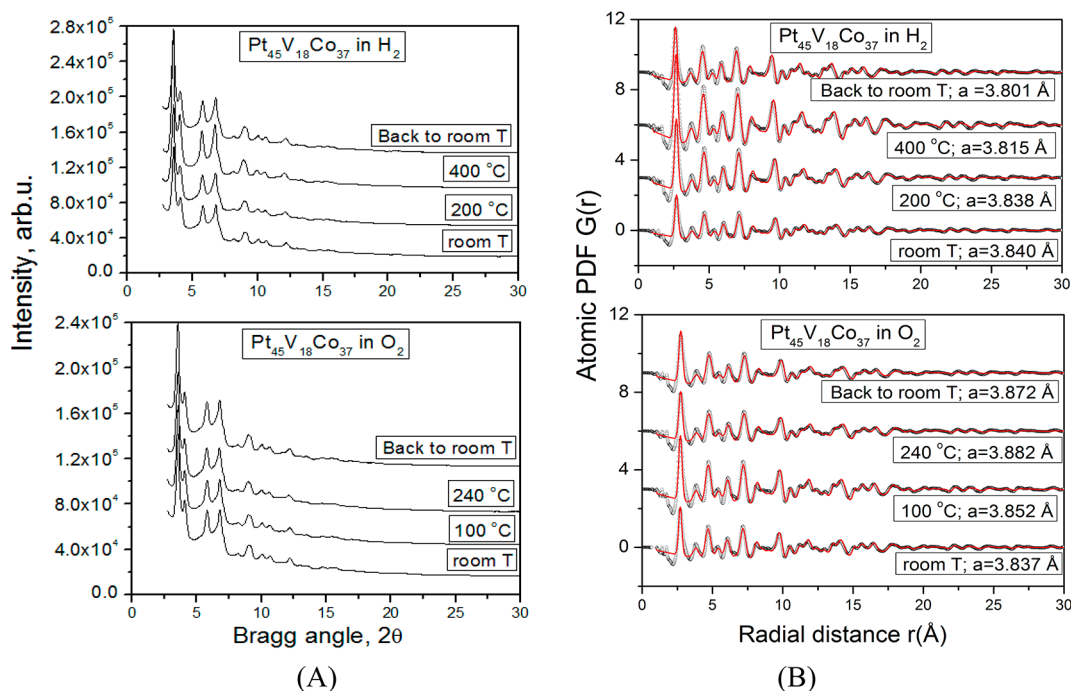


Figure 7. (A) Experimental in situ XRD data for Pt₄₅V₁₈Co₃₇/C taken with X-rays of wavelength 0.13702 Å. (B) Experimental (symbols) and model (line in red) atomic PDFs. The refined fcc lattice parameter is shown by each data set. Fresh sample Pt₄₅V₁₈Co₃₇/C (prepared by treatment at 260 °C under 20 vol % O₂ followed by treatment at 400 °C in 15 vol % H₂) was tested under 10 vol % O₂ followed by 3.5 vol % H₂ balanced by He.

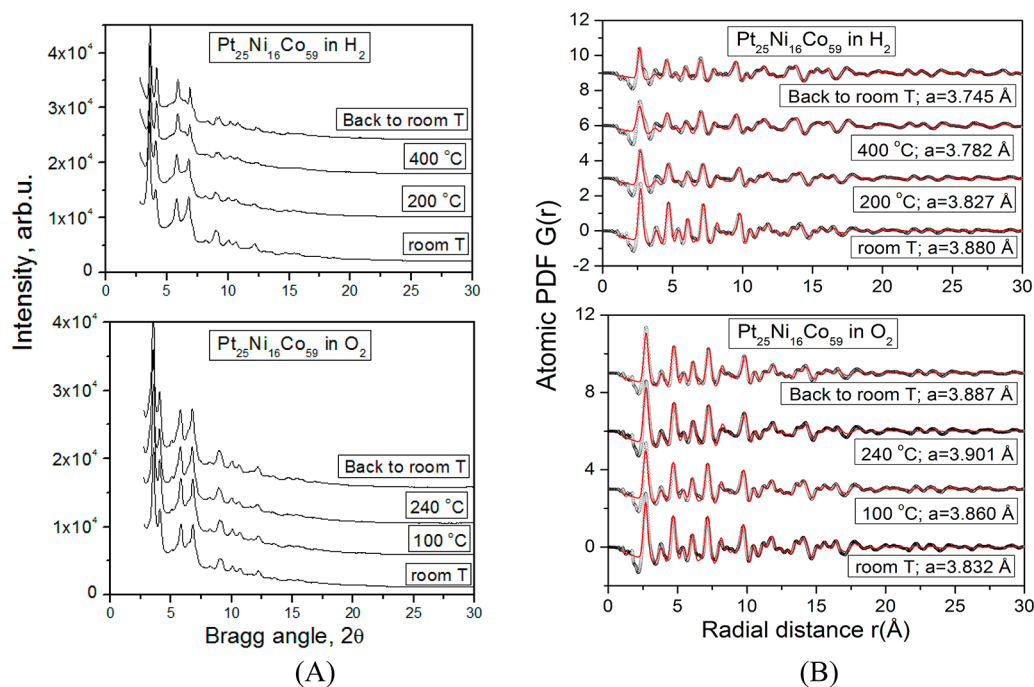


Figure 8. (A) Experimental in situ HE-XRD data for Pt₂₅Ni₁₆Co₅₉/C taken with X-rays of wavelength 0.13702 Å. (B) Experimental (symbols) and model (line in red) atomic PDFs. The refined fcc lattice parameter is shown by each data set.

lattice parameter of the PtVCo catalyst are only half of those observed for the PtNiCo system. In other words, PtVCo maintains a more stable lattice parameter, i.e., a more stable atomic scale structure, than the PtNiCo system in the catalytic reaction process.

As reported in our recent study,⁷ the Pt₂₅Ni₁₆Co₅₉/C nanoalloy's interatomic distances increase when the catalyst is treated in oxidizing atmosphere, and shrink uniformly when the

catalyst is treated in reducing atmosphere. The nanoalloy particles remain “expanded” when cooled back to room temperature in oxidizing atmosphere, and “shrunk” if cooled back to room temperature in reducing atmosphere. The expansion of the interatomic distances upon oxidation is consistent with the enhanced interaction of oxygen with the particle's surface that is favored by the oxophilicity of the base transition metal. The overall shrinking of the interatomic

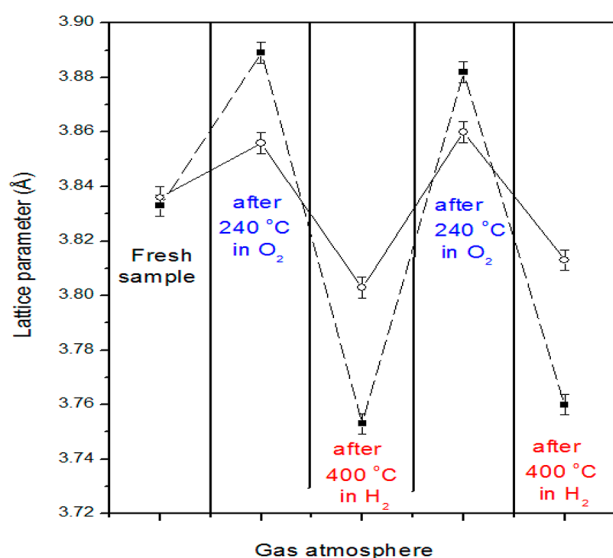


Figure 9. Evolution of the fcc-lattice parameter of Pt₄₅V₁₈Co₃₇ (open circles) and Pt₂₅Ni₁₆Co₃₉ (black squares) in the thermochemical treatment cycles in O₂ (at 240 °C) and H₂ (400 °C) atmosphere, as denoted on the horizontal axis, and then cooled down to RT.

distances in the nanoalloy particles treated in a reducing atmosphere is consistent with freeing the oxygenated species. The Pt₂₅Ni₁₆Co₃₉/C features chemically disordered (random alloy) structure.

An ex situ study of Pt₂₃Ir₂₉Co₄₈/C catalysts was also performed, and the atomic PDFs revealed a shrinking of the lattice parameter from 3.797 to 3.737 Å with increasing the temperature of treatment from 400 to 800 °C in reductive (H₂) gas. In comparison, a shrinking of the lattice parameter is observed from 3.874 Å at 400 °C to 3.867 Å at 800 °C for a PtCo/C. For Pt₂₃Ir₂₉Co₄₈/C catalyst processed at 400 °C, a structure model constructed by reverse Monte Carlo simulations features an alloy where Co and Ir species tend to occupy the inner part of the nanoparticles while Pt atoms show some preference for being closer to the surface of the nanoparticles. In contrast, for Pt₂₃Ir₂₉Co₄₈/C catalyst processed at 800 °C, the RMC model features a rather, but not completely, random type of alloy where Co, Pt, and Ir atoms are almost uniformly distributed across the nanoparticles.³⁰

Table 2 summarizes the changes of the lattice parameters for the Pt₄₅V₁₈Co₃₇/C catalysts under different conditions. There is a clear lattice expansion upon oxidation ($\Delta a/a = 0.9\%$) and lattice shrinking upon reduction ($\Delta a/a = -1.0\%$). Under CO reaction conditions (80 °C, 2.5 vol % CO + 10 vol % O₂), the

change in the lattice parameter is very small (<0.1%). Upon reductive treatment following the catalytic reaction, there is a small lattice parameter shrinking (−0.5%). It may be conjectured that the insignificant change of the lattice parameter under the catalytic reaction condition is indicative of a surface self-regulation of the oxygenated species by the second and third transition metals (V and Co) in the PtVCo nanoalloy.

In comparison, the lattice expansion upon oxidation ($\Delta a/a = 1.4\%$) and shrinking upon reduction ($\Delta a/a = -3.6\%$) are somewhat larger for the PtNiCo catalyst (Table 2). However, under catalytic reaction conditions (80 °C, 2.5 vol % CO + 10 vol % O₂), the lattice expansion is also very small (~0.03%). Upon reductive treatment after the catalytic reaction, there is also a small lattice shrinking (−0.2%). These changes are apparently quite similar to those observed for the PtVCo nanoalloy. A major contrast between the PtNiCo and PtVCo nanoalloys under the catalytic reaction condition is that the PtNiCo has a lattice constant (3.886 Å) larger than that for the PtVCo nanoalloy (3.844 Å). The fact that the PtNiCo has a lower catalytic activity than that for the PtVCo is therefore believed to be associated with the larger lattice constant of PtNiCo under the catalytic reaction condition and its greater tendency of lattice expansion/shrinking under the O₂/H₂ conditions.

It is important to further note that, for the nanoalloys in the reducing atmosphere (H₂) and in the CO oxidation atmosphere, there is no indication of phase segregation of the nanoalloy. This assessment is supported mainly by both ex situ and in situ synchrotron HE-XRD/PDF data, which, unlike regular XRD, can detect structural changes for both crystalline and amorphous samples. A comparison of the lattice parameters determined by HE-XRD/PDF for PtVCo and PtCo samples (Tables S3–4, Supporting Information) showed clear differences in terms of the relative changes of the lattices between the data before and after O₂ treatments, and between the data after O₂ and H₂ treatments. These differences can be explained by an increased tendency of oxygen insertion in the PtVCo structure upon oxidation in comparison with PtCo because of a greater oxophilicity of V than that of Co due to V being a part of the PtVCo nanoalloy. This finding is consistent with a significant difference in electrocatalytic activity observed for oxygen reduction reaction between PtVCo and PtCo,^{6,18,21} which is dictated by the catalytic sites associated with Pt and its alloy.

The catalysts were also analyzed by ex situ XAFS and XPS techniques.^{6,7,18,21} To further understand the effects of the oxidative or reductive treatments on the catalyst structure,

Table 2. Lattice Parameters (*a*) Derived from the HE-XRD/PDF Analysis Results^a

catalyst	sample treatment	<i>a</i> (R _i)/Å	<i>a</i> (R _f)/Å	<i>a</i> (H)/Å	$\Delta a/a$
Pt ₄₅ V ₁₈ Co ₃₇	240 O ₂	3.837	3.872	3.882	0.9%
	400 H ₂	3.840	3.801	3.815	−1.0%
	80 °C, 0.5% CO + 10% O ₂	3.842	3.844	3.845	~0.05%
	400 H ₂	3.850	3.831	3.848	~−0.5%
Pt ₂₅ Ni ₁₆ Co ₃₉	240 O ₂	3.832	3.887	3.901	1.4%
	400 H ₂	3.880	3.745	3.782	−3.6%
	80 °C, 0.5% CO + 10% O ₂	3.885	3.886	3.887	~0.03%
	400 H ₂	3.861	3.851	3.828	−0.2%
Pt ₂₃ Ir ₂₉ Co ₄₈	400 H ₂	3.797			

^aNote: H, the highest temperature tested; R, room temperature (25 °C) (R_i, initial; R_f, final room temperature). $\Delta a/a = (a(R_f) - a(R_i))/a(R_i)$.

XAFS and XPS analyses were also performed for the Pt₄₅V₁₈Co₃₇/C nanoalloys treated in oxidative (O₂) and reductive (H₂) gas at different temperatures, in comparison with PtNiCo/C and PtIrCo/C (see Tables S5–6, Supporting Information).^{7,18} In general, the results reveal the presence of oxygenated species largely associated with the presence of high oxidation states of the transition metals, as reflected by the increased M–O coordination numbers. The results support the assessment of the structural changes as a result of the introduction of the M/M's in the nanoalloys.

4. CONCLUSION

Taken together, the results suggest that self-tunable oxophilicity and structural integrity of the PtVCo nanoalloy catalysts, i.e., little variance of the lattice parameter, may be very important factors for the significant enhancement of the catalytic activities for CO oxidation. The introduction of a third transition metal (M' = V, Ni, Ir, etc.) into PtCo nanoalloys minimizes or suppresses changes in the lattice parameters of the nanoparticle during the catalytic processes, leading to an activity enhancement in the order of V > Ni > Ir, consistent with the order of oxophilicity of these metals. The HE-XRD/PDF results have revealed a significant contrast of the lattice expansion and shrinking between M' = V and Ni in the nanoalloys under the oxidation/reductive and catalytic reaction conditions. The lattice expansion and shrinking under CO oxidation condition are very small for PtVCo, whereas the lattice changes in PtNiCo are larger than PtVCo. In addition to explaining why the catalytic activity of PtNiCo is lower than that of PtVCo, this finding provides a new physical insight into the role of the metal component's oxophilicity in controlling the nanoalloy structure under the reactive conditions. An in-depth understanding of how the change of the lattice parameter under the reaction condition and the reductive condition can be precisely controlled for achieving the optimal surface self-regulation of the oxygenated species by the second and third transition metals in other nanoalloys is an important subject of our ongoing investigations.

■ ASSOCIATED CONTENT

Supporting Information

Additional scheme, HE-XRD, XAFS, XPS, and experimental data. This material is available free of charge via the Internet at <http://pubs.acs.org>.

■ AUTHOR INFORMATION

Corresponding Author

*E-mail: cjzhong@binghamton.edu.

Notes

The authors declare no competing financial interest.

■ ACKNOWLEDGMENTS

This work was supported by the DOE-BES Grants DE-SC0006877 and in part by the National Science Foundation (CMMI-1100736). Work at the Advanced Photon Source was supported by DOE under Contract DE-AC02-06CH11357. Thanks are also due to beamline 11-ID-B and 11-ID-C staff for the help with the HE-XRD experiments.

■ REFERENCES

(1) Date, M.; Ichihashi, Y.; Yamashita, T.; Chiorino, A.; Bocuzzi, F.; Haruta, A. *Catal. Today* **2002**, *72*, 89–94.

(2) Wang, C.; Yin, H. G.; Chan, R.; Peng, S.; Dai, S.; Sun, S. H. *Chem. Mater.* **2009**, *21*, 433–435.

(3) Haruta, M.; Tsubota, S.; Kobayashi, T.; Kageyama, H.; Genet, M. J.; Delmon, B. *J. Catal.* **1993**, *144*, 175–192.

(4) Wanjala, B. N.; Loukrakpam, R.; Luo, J.; Njoki, P. N.; Mott, D.; Zhong, C. J.; Shao, M. H.; Protsailo, L.; Kawamura, T. *J. Phys. Chem. C* **2010**, *114*, 17580–17590.

(5) Wanjala, B. N.; Fang, B.; Luo, J.; Chen, Y. S.; Yin, J.; Engelhard, M. H.; Loukrakpam, R.; Zhong, C. J. *J. Am. Chem. Soc.* **2011**, *133*, 12714–12727.

(6) Wanjala, B. N.; Fang, B.; Loukrakpam, R.; Chen, Y. S.; Engelhard, M.; Luo, J.; Yin, J.; Yang, L. F.; Shan, S.; Zhong, C. J. *ACS Catal.* **2012**, *2*, 795–806.

(7) Yang, L. F.; Shan, S.; Loukrakpam, R.; Petkov, V.; Ren, Y.; Wanjala, B. N.; Engelhard, M. H.; Luo, J.; Yin, J.; Chen, Y. S.; Zhong, C. J. *J. Am. Chem. Soc.* **2012**, *134*, 15048–15060.

(8) Crans, D. C. *Pure Appl. Chem.* **2005**, *77*, 1497–1527.

(9) Xie, X.; Li, Y.; Liu, Z. Q.; Haruta, M.; Shen, W. *Nature* **2009**, *458*, 746–749.

(10) Stamenkovic, V.; Mun, B. S.; Mayrhofer, K. J.; Ross, P. N.; Markovic, N. M.; Rossmeisl, J.; Greeley, J.; Norskov, J. K. *Angew. Chem., Int. Ed.* **2006**, *45*, 2897–2901.

(11) Xin, H. L.; Holewinski, A.; Linic, S. *ACS Catal.* **2012**, *2*, 12–16.

(12) Wang, L.; Williams, J. I.; Lin, T.; Zhong, C. J. *Catal. Today* **2011**, *165*, 150–159.

(13) Fernandez, J. L.; Walsh, D. A.; Bard, A. J. *J. Am. Chem. Soc.* **2005**, *127*, 357–365.

(14) Nørskov, J. K.; Rossmeisl, J.; Logadottir, A.; Lindqvist, L.; Kitchin, J. R.; Bligaard, T.; Jonsson, H. *J. Phys. Chem. B* **2004**, *108*, 17886–17892.

(15) Hwang, S. J.; Yoo, S. J.; Jang, S.; Lim, T.-H.; Hong, S. A.; Kim, S.-K. *J. Phys. Chem. C* **2011**, *115*, 2483–2488.

(16) Zhang, Y. H.; Duan, Z. Y.; Xiao, C.; Wang, G. F. *Surf. Sci.* **2011**, *605*, 1577–1582.

(17) Yin, J.; Shan, S. Y.; Yang, L. F.; Mott, D.; Malis, O.; Petkov, V.; Cai, F.; Ng, M. S.; Luo, J.; Chen, B. H.; Engelhard, M.; Zhong, C. J. *Chem. Mater.* **2012**, *24*, 4662–4674.

(18) Loukrakpam, R.; Wanjala, B. N.; Yin, J.; Fang, B.; Luo, J.; Shao, M. H.; Protsailo, L.; Kawamura, T.; Chen, Y. S.; Petkov, V.; Zhong, C. J. *ACS Catal.* **2011**, *1*, 562–572.

(19) Petkov, V.; Yang, L.; Yin, J.; Loukrakpam, R.; Shan, S.; Wanjala, B.; Luo, J.; Chapman, K. W.; Zhong, C. J. *Phys. Rev. Lett.* **2012**, *109*, 125504.

(20) Petkov, V.; Shan, S.; Chupas, P.; Yin, J.; Yang, L.; Luo, J.; Zhong, C. J. *Nanoscale* **2013**, *5*, 7379–7387.

(21) Wanjala, B. N.; Fang, B.; Shan, S. Y.; Petkov, V.; Zhu, P. Y.; Loukrakpam, R.; Chen, Y. S.; Luo, J.; Yin, J.; Yang, L. F.; Shao, M. H.; Zhong, C. J. *Chem. Mater.* **2012**, *24*, 4283–4293.

(22) Loukrakpam, R.; Luo, J.; He, T.; Chen, Y. S.; Xu, Z. C.; Njoki, P. N.; Wanjala, B. N.; Fang, B.; Mott, D.; Yin, J.; Klar, J.; Powell, B.; Zhong, C. J. *J. Phys. Chem. C* **2011**, *115*, 1682–1694.

(23) Luo, J.; Kariuki, N.; Han, L.; Wang, L.; Zhong, C. J.; He, T. *Electrochim. Acta* **2006**, *51*, 4821–4827.

(24) Oxford, S. M.; Lee, P. L.; Chupas, P. J.; Chapman, K. W.; Kung, M. C.; Kung, H. H. *J. Phys. Chem. C* **2010**, *114*, 17085–17091.

(25) Egami, T.; Billinge, S. J. L. *Underneath the Bragg's Peak*; Pergamon: Amsterdam, The Netherlands, 2003.

(26) Petkov, V. *Mater. Today* **2008**, *11*, 28–38.

(27) Petkov, V.; Bedford, N.; Knecht, M. R.; Weir, M. G.; Crooks, R. M.; Tang, W.; Henkelman, G.; Frenkel, A. *J. Phys. Chem. C* **2008**, *112*, 8907–8911.

(28) Huang, W. J.; Sun, R.; Tao, J.; Menard, L. D.; Nuzzo, R. G.; Zuo, J. M. *Nat. Mater.* **2008**, *7*, 308–313.

(29) Farrow, C. L.; Juhás, P.; Liu, J. W.; Bryndin, D.; Božin, E. S.; Bloch, J.; Proffen, Th.; Billinge, S. J. L. *J. Phys.: Condens. Matter* **2007**, *19*, 335219.

(30) Loukrakpam, R.; Shan, S.; Petkov, V.; Yang, L.; Luo, J.; Zhong, C. J. *J. Phys. Chem. C* **2013**, *117*, 20715–20721.